Engineered gold/black phosphorus nanoplatforms with remodeling tumor microenvironment for sonoactivated catalytic tumor theranostics

Ting Chen [a,1], Weiwei Zeng [a,1], Changjun Tie [b], Mian Yu [a], Huisong Hao [a], Yang Deng [a], Qianqian Li [a,c], Hairong Zheng [b,***], Meiying Wu [a,**], Lin Mei [a,c,*]

[a] *School of Pharmaceutical Sciences (Shenzhen), Sun Yat-sen University, Shenzhen, 518107, China*
[b] *Paul C. Lauterbur Research Center for Biomedical Imaging, Institute of Biomedical and Health Engineering, Shenzhen Institutes of Advanced Technology, Chinese Academy of Sciences, Shenzhen, 518055, China*
[c] *Tianjin Key Laboratory of Biomedical Materials, Key Laboratory of Biomaterials and Nanotechnology for Cancer Immunotherapy, Institute of Biomedical Engineering, Chinese Academy of Medical Sciences, Peking Union Medical College, Tianjin, 300192, China*

ABSTRACT

The imbalance between oxidants and antioxidants in cancer cells would evoke oxidative stress-induced cell death, which has been demonstrated to be highly effective in treating malignant tumors. Sonodynamic therapy (SDT) adopts ultrasound (US) as the excitation source to induce the production of reactive oxygen species (ROS), which emerges as a noninvasive therapeutic strategy with deep tissue penetration depth and high clinical safety. Herein, we construct novel sonoactivated oxidative stress amplification nanoplatforms by coating MnO_2 on Au nanoparticle-anchored black phosphorus nanosheets and decorating soybean phospholipid subsequently (Au/BP@MS). The Au/BP@MS exhibit increased ROS generation efficiency under US irradiation in tumor tissues due to Au/BP nanosensitizer-induced improvement of electron-hole separation as well as MnO_2-mediated O_2 generation and GSH depletion, thus leading to notable inhibition effect on tumor growth. Moreover, tumor microenvironment-responsive biodegradability of Au/BP@MS endows them with enhanced magnetic resonance imaging guidance and clinical potential for cancer theranostics.

1. Introduction

Redox homeostasis is of great significance to maintain the various normal physiological functions of the organism [1]. Disturbance in this balance can induce genetic mutations, metabolic abnormalities, and alteration in the microenvironments, thus leading to the occurrence of many diseases, such as cancers [2–4]. Although moderate levels of ROS in cancer cells have been considered to be associated with the development of cancer, excessive accumulation of intracellular ROS above a threshold can induce cell death by damaging nucleic acids, lipids, proteins, and other cellular constituents. Recently, amplified intracellular oxidative stress has been developed as an effective strategy to fight against cancer by promoting ROS generation and/or antioxidant depletion [5].

SDT is a newly emerging noninvasive therapeutic modality, which utilizes low-intensity focused US to activate sonosensitizers to realize ROS-inducing apoptosis or necrosis [6–8]. Similar to clinically used photodynamic therapy (PDT), sensitizing agents, O_2, and exogenous stimuli are the indispensable components in producing ROS for tumor-specific treatment. Unlike PDT, which uses laser irradiation, SDT employs US exposure as the excitation source, thus endowing SDT with excellent clinical prospect due to the deeper tissue-penetrating depth of US in comparison with laser [9,10]. The originally validated sonosensitizers are organic photosensitizer molecules, such as porphyrins and their derivatives [11,12]. However, their low chemical and biological stability, and rapid body clearance compromise the efficacy of sonoactivated catalytic tumor eradication [13]. With the remarkable advances in nanobiotechnology, various approaches have been

---

developed to solve these problems, including transport or linkage of organic sonosensitizers to nanomaterials and development of novel inorganic sonosensitizers [7,14]. The most typical inorganic sonosensitizer is titanium dioxide, however, its poor $^1O_2$ production capability derived from the rapid recombination of electron-hole pairs as well as its non-biodegradable characteristic hinder its further clinical translation [15,16]. Black phosphorus (BP) nanosheet, a fascinating 2D nanomaterial composing of elemental phosphorus, has displayed versatile biological effects against cancer with high biodegradability, biocompatibility, and specificity [17–20]. Despite BP-based photodynamic and photothermal therapies have been extensively investigated, its sonosensitizing effect is still in its infancy [21–23]. Recent study has shown that BP nanosheet as the piezoelectric material can be polarized by US and exhibits US-excited cytotoxicity via ROS generation, demonstrating its potential as a novel sonosensitizer [24].

Apart from exploiting highly efficient sonosensitizers, remodeling tumor microenvironment (TME) is also a powerful means to potentiate SDT efficacy as the hypoxic and glutathione (GSH)-rich TME can significantly attenuate the $^1O_2$ production efficiency [25]. Moreover, it has been suggested that manganese oxide (MnO_2) nanosystems could simultaneously achieve TME-specific O_2 generation, GSH depletion, and biodegradability [26–28]. Inspiringly, herein, we explore a novel intelligent SDT nanoplatform with good physiological stability and biocompatibility for highly efficient and magnetic resonance (MR) imaging-guided sonoactivated catalytic tumor therapy by anchoring gold nanoparticles (Au NPs) on the surface of 2D layered BP, coating MnO_2 shell and modifying soybean phospholipid (SP) subsequently (Au/BP@MS, Fig. 1A). The unique energy band structures, thickness-dependent band gaps, and semiconductor features of BP nanosheets made them hold huge potential for the separation of electron-hole pairs under exposure of exogenous US [19,29]. Moreover, their high specific surface areas and reductive properties guaranteed the high anchoring amounts of Au NPs which would trap the excited electrons due to the surface plasmon resonance, thus inhibiting the rapid recombination of electron-hole pairs for enhanced SDT [30,31]. Additionally, the remarkable alleviation of tumor hypoxia and depletion of antioxidants achieved by MnO_2 shell would cause intracellular oxidative stress amplification and synergistically strengthen SDT efficacy [32,33]. The simultaneous release of Mn^{2+} derived from pH-sensitive biodegradation would function as T_1-weighted MR imaging agents for enhanced tumor-specific imaging and detection [32,34]. Importantly, TME-responsive biodegradable character of Au/BP@MS ensured significantly enhanced tumor specificity and biosafety *in vivo* (Fig. 1B).
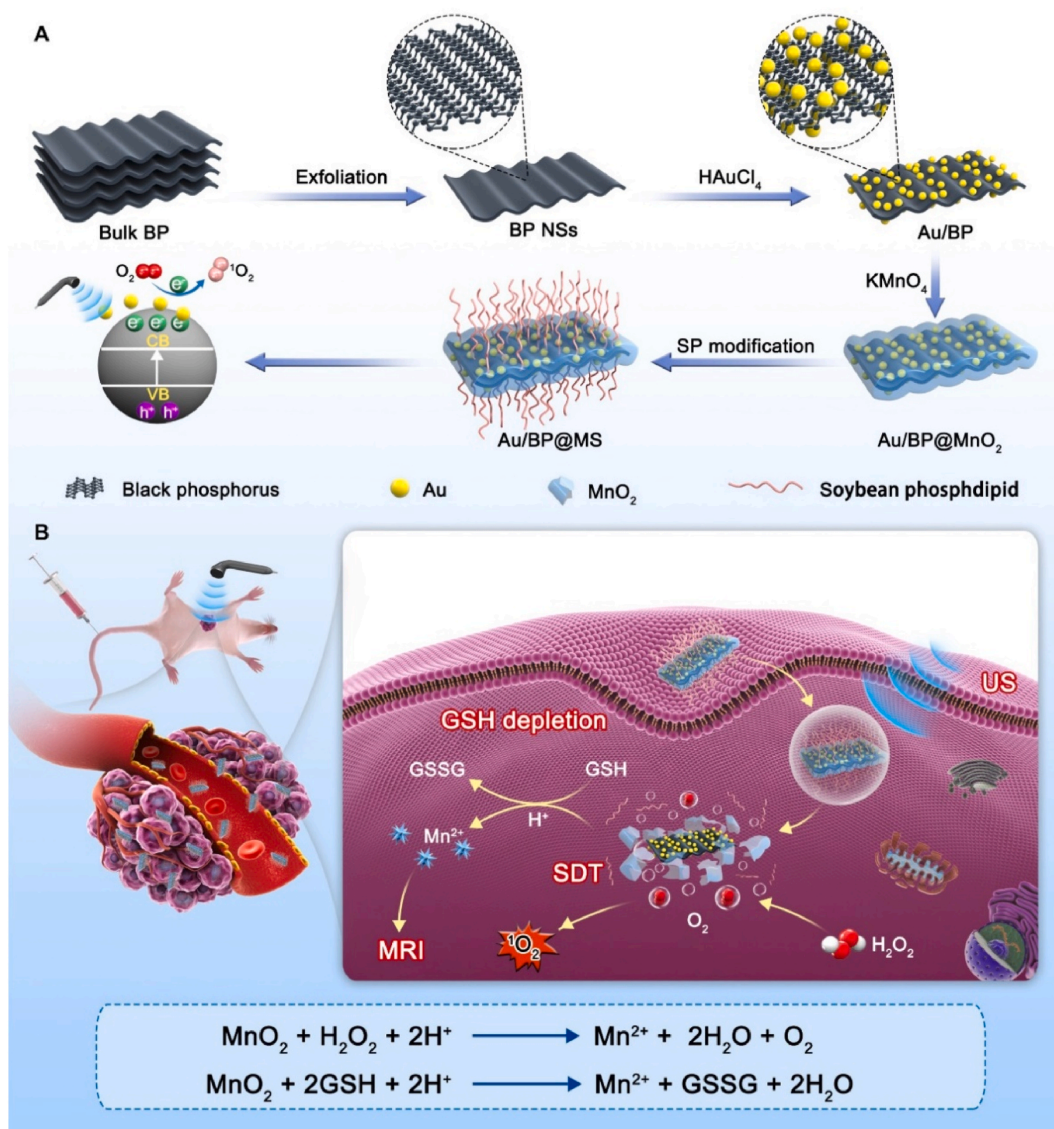

Fig. 1. (A) Schematically illustration of preparation and (B) sonoactivated catalytic tumor theranostics of Au/BP@MS.

2. Materials and methods

2.1. Materials

Black phosphorus crystals were purchased from Nanjing Muke Nano Technology Co., Ltd. Gold (III) chloride trihydrate (HAuCl$_4$·3H$_2$O) was obtained from Sigma-Aldrich. Potassium permanganate (KMnO$_4$) was obtained from Sinopharm Chemical Reagent Co., Ltd. (Guangzhou, China). Soybean phospholipid (SP) was purchased from Xi'an Ruixi Biochemistry Technology CO., Ltd. N-methyl-2-pyrrolidone (NMP) was purchased from Aladdin (Shanghai, China). All other chemicals and reagents were of the highest quality commercially available and used as received.

2.2. Synthesis of Au/BP@MS

BP nanosheets were prepared by a modified liquid exfoliation. Briefly, bulk BP crystals was added to NMP (0.5 mg/mL), then was sonicated with a sonic tip for 20 h (600 W). The resulting brown suspension was centrifuged at 5000 rpm for 15 min and the supernatant was further centrifuged at 14,000 rpm for 15 min to collect nanosheets of appropriate size. The collected BP nanosheets were redispersed in deionized water, HAuCl$_4$ aqueous solution (100 μg/mL) was added into the BP nanosheet dispersion (100 μg/mL) and the mixture was ultrasonicated for 10 min. The resulting product was acquired after three times of centrifugation (12,000 rpm, 10 min). KMnO$_4$ (200 μg/mL) was added dropwise to the solution containing Au/BP under mild stirring. Then, the mixture was stirred vigorously at 40 °C for 1 h. The resulting Au/BP@MnO$_2$ were acquired after two times of centrifugation (12,000 rpm, 10 min) and redispersed in ethanol. As for the modification with SP, SP was dissolved in of CHCl$_3$ (500 μg/mL), followed by the addition of Au/BP@MnO$_2$ nanosheets (1 mg/mL). After sonication for 10 min, the solution was incubated in a rotary evaporator at 40 °C to evaporate the solvent. The obtained Au/BP@MS were dispersed in phosphate buffer solution (PBS) for further use.

2.3. In vitro O$_2$ and ^{1}O$_2$ generation

The dissolved O$_2$ concentrations in PBS were measured by a JPSJ-605F portable dissolved oxygen meter (Leici Instrument Co., Ltd, Shanghai, China). Briefly, Au/BP@MS (50 μg/mL) was redispersed in PBS (pH 7.4 or 6.5) and further filled with argon and sealed with parafilm. Then the real-time O$_2$ concentrations were recorded after injection of H$_2$O$_2$ (100 μM). Meanwhile, the O$_2$ concentrations of Au/BP (the same Au/BP amount with Au/BP@MS) under the same conditions were measured as the control group.

To detect US-triggered ^{1}O$_2$ generation, Au/BP (25 μg/mL) or Au/BP@MS (50 μg/mL) was mixed with H$_2$O$_2$ (100 μM). After adding SOSG (10 μM), the mixture was exposed to US irradiation (1.0 MHz, 1.0 W/cm^2, 50% duty cycle) for different durations. Then the fluorescence intensity of the mixture was measured by a fluorescence spectrophotometer (Ex/Em: 488/525 nm). In the meanwhile, deionized water and pure BP nanosheets (10 μg/mL based on the content of P element) mixed with H$_2$O$_2$ (100 μM) were also detected.

2.4. In vitro GSH depletion

The consumption of GSH was monitored by UV–vis spectroscopy. Au/BP@MS (50 μg/mL) were mixed with GSH (1 mM) at room temperature. At different time points, the solution was taken out and mixed with 675 μL PBS, and then 5, 5′-dithiobis-(2-nitrobenzoic acid) (DTNB) (10 mg/mL) was added. The absorbance spectrum of the supernatant was measured by UV–vis spectroscopy. Deionized water, pure BP nanosheets (10 μg/mL based on the content of P element), Au/BP nanosheets (25 μg/mL) at the same conditions were measured.

2.5. Cell culture

Human breast carcinoma cell line MCF-7 was obtained from the American Type Culture Collection. The cells were cultured in high glucose Dulbecco's modified Eagle medium (DMEM) supplemented with 10% fetal bovine serum and 1% penicillin-streptomycin at 37 °C under an atmosphere of 5% CO$_2$.

2.6. Cellular uptake

To investigate the cellular internalization profile of Au/BP@MS, MCF-7 cells were seeded in the confocal dish with a density of 2×10^5 cells and cultured overnight, and then co-incubated with Cy5-labeled Au/BP@MS (the concentration of Cy5 was 5 μg/mL) for different time points (0.5, 1.5, 3, and 6 h) at 37 °C. At the end of incubation, the redundant media were removed by washing with PBS three times. Afterward, the cells were fixed with 4% paraformaldehyde solution and stained by 4',6-diamidino-2-phenylindole (DAPI), followed by observation under a confocal laser scanning microscope (LSN880, Zeiss, Germany). Furthermore, flow cytometry (CytoFLEX, Beckman coulter, USA) was also used to quantitatively detect the cellular uptake, wherein MCF-7 cells were treated as described above.

2.7. In vitro cytotoxicity assay

The cytotoxicity of Au/BP@MS nanosheets against MCF-7 cancer cells was evaluated by standard Cell Counting Kit-8 (CCK-8) assay. For the in vitro cell toxicity test, MCF-7 cells were seeded in 96-well plates with a density of 8×10^3 cells per well and cultured for 12 h. After washing once with PBS, the cells were incubated with elevated concentrations (0, 6.25, 12.5, 25, 50, and 75 μg/mL) of Au/BP@MS or corresponding concentrations (0, 3.125, 6.25, 12.5, 25, and 37.5 μg/mL) of Au/BP for 24 h. After washing with PBS, the typical CCK-8 kit was used to determine the relative cell viabilities.

For the in vitro SDT, MCF-7 cells were seeded in 96-well plates with a density of 8×10^3 cells per well for 12 h. After washing once with PBS, the cells were incubated with elevated concentrations (0, 6.25, 12.5, 25, 50, and 75 μg/mL) of Au/BP@MS or corresponding concentrations (0, 3.125, 6.25, 12.5, 25, and 37.5 μg/mL) of Au/BP for 6 h and washed with PBS. Then, the cells were exposed to US irradiation (1.0 MHz, 1.0 W/cm^2, 50% duty cycle) for 3 min and further incubated for 18 h. The standard CCK-8 test was conducted to determine the cell viability.

The amounts of live/dead cells were further determined by using a Live/Dead Calcein-AM/PI Double Stain Kit. Briefly, MCF-7 cells (1 × 10^5 cells per well) were firstly seeded in 12-well plates and cultured overnight. Afterward, the media were replaced by fresh DMEM (control group, US group), Au/BP (25 μg/mL) or Au/BP@MS (50 μg/mL). After incubation for 6 h, the cells in US, Au/BP + US, and Au/BP@MS + US groups were exposed to US irradiation (1.0 MHz, 1.0 W/cm^2, 50% duty cycle) for 3 min, and continued to culture for another 12 h. Finally, the cells were stained with calcein-AM/PI solution for 20 min and observed by fluorescence microscope (DMIRB, Leica, Germany).

2.8. Intracellular ROS generation, GSH depletion, and mitochondrial membrane potential

MCF-7 cells were seeded in the confocal dish with a density of 2×10^5 cells and cultured overnight, then co-cultured with fresh DMEM, Au/BP (25 μg/mL), or Au/BP@MS (50 μg/mL) for 6 h. The cells in US, Au/BP + US, and Au/BP@MS + US groups were exposed to US irradiation (1.0 MHz, 1.0 W/cm^2, 50% duty cycle) for 3 min. For in vitro ROS detection, the cells were stained with DCFH-DA (20 μM) for 30 min. For in vitro GSH detection, the cells were stained with ThiolTracker™ Violet (20 μM) for 30 min. Mitochondrial membrane potential assay was conducted by JC-1 kit. All the images were acquired by Confocal Laser Scanning Microscope (LSN880, Zeiss, Germany).

2.9. Animal model

Female Balb/c nude mice (16–18 g, 4–5 weeks old) were purchased from Guangdong Medical Laboratory Animal Center (Guangzhou, China). All animal experiments were performed according to the guidelines approved by the Institutional Animal Care and Use Committee of Sun Yat-sen University (Guangzhou, China). 2×10^6 MCF-7 cells were subcutaneously injected into the forelimb chest of Balb/c nude mice. When the tumor became distinct and the tumor volume reached ~100 mm^3, the mice were randomly assigned into six groups.

2.10. T_1-weighted MR imaging and in vivo biological distribution study

Au/BP@MS with various Mn concentrations were dispersed in the different buffer solutions (pH = 5.5 or 7.4, [GSH] = 0 or 10 mM, [H$_2$O$_2$] = 0 or 100 μM) for 2 h at 37 °C under mild shaking. Then, the Au/BP@MS solutions in Eppendorf tubes (1 mL volume) were performed for MR scanning. For *in vivo* MR imaging, before and after the intravenous injection of Au/BP@MS ([Mn] = 50 mM), the mice were scanned by a 3.0 T clinical MRI scanner (UNITED IMAGING) with a special coil for small animal imaging.

As for *in vivo* fluorescence imaging and biodistribution of Cy5-labeled Au/BP@MS. After the intravenous injection of free Cy5 or Cy5-labeled Au/BP@MS (2.5 mg/kg Cy5 per mouse), the mice were measured by the *In vivo* Imaging System (NightOWL II LB983, Germany) at different time points (0, 2, 4, 8, 12, and 24 h). Then, the main organs (heart, liver, spleen, lung, and kidney) and tumors were collected and imaged immediately. The fluorescence intensities of Cy5 in tumors and
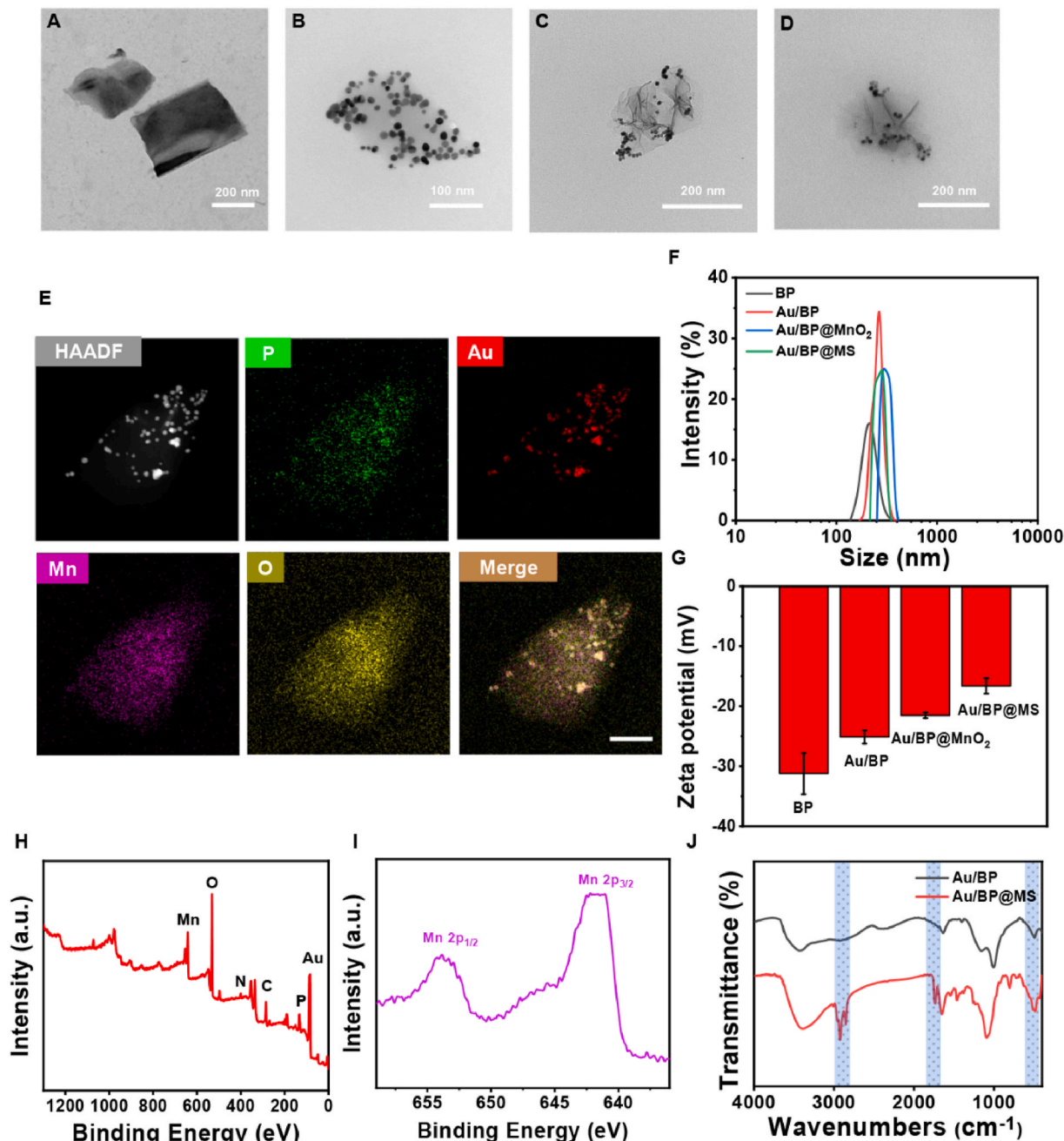

Fig. 2. Synthesis and characterization of Au/BP@MS. TEM images of (A) BP, (B) Au/BP, (C) Au/BP@MnO$_2$, and (D) Au/BP@MS. (E) HAADF-STEM image and corresponding elemental mapping images of Au/BP@MnO$_2$. Scale bar = 100 nm. (F) Hydrodynamic size and (G) zeta potential of BP, Au/BP, Au/BP@MnO$_2$, and Au/BP@MS. (H) XPS spectrum of Au/BP@MS. (I) High-resolution Mn 2p XPS spectrum of Au/BP@MS. (J) FTIR spectra of Au/BP and Au/BP@MS.

main organs were quantified.

2.11. In vivo antitumor efficacy

To investigate the antitumor efficacy of Au/BP@MS, tumor-bearing nude mice were divided into six groups (n = 5): (Group 1) control; (Group 2) US alone; (Group 3) Au/BP (i.v. injection, 7.5 mg/kg); (Group 4) Au/BP + US (i.v. injection, 7.5 mg/kg); (Group 5) Au/BP@MS (i.v. injection, 15 mg/kg Au/BP@MS is equivalent to 7.5 mg/kg Au/BP); (Group 6) Au/BP@MS + US (i.v. injection, 15 mg/kg). These mice received three injections on day 1, 3, and 5. At 12 h post i.v. injection, the mice in the Group (2), (4), and (6) were exposed to US irradiation (1 MHz, 1 W/cm^2, 5 min, 50% duty cycle), which was repeated once on the following day. In the meanwhile, the tumor length and width were recorded to calculate the volume of tumors by the formula: Volume = (Length × Width^2)/2. 14 days later, the mice were sacrificed and the main organs (heart, liver, spleen, lung, kidney, and tumor) were collected for histological analysis.

3. Results and discussion

3.1. Synthesis and characterization of Au/BP@MS nanosheets

The ultrathin BP nanosheets were successfully prepared by a simple liquid-phase exfoliation method and employed as the self-sacrificed templates for the reduction reactions with HAuCl$_4$ and KMnO$_4$ to establish Au/BP@MnO$_2$ nanoplatforms. Afterward, the coating of SP layer on the surface of Au/BP@MnO$_2$ via a rotary-evaporation technique contributed to the formation of Au/BP@MS nanosheets, which endowed high dispersibility and physiological stability. The synthesized BP, Au/BP, Au/BP@MnO$_2$, and Au/BP@MS nanosheets all exhibited an ultrathin 2D morphology, as visualized under the transmission electron microscope (TEM, Fig. 2A–D). The chemical component of Au/BP@MnO$_2$ was investigated by high-angle annular dark-field scanning TEM (HAADF-STEM) and energy-dispersive X-ray spectroscopy. As shown in Fig. 2E and S1, the coexistence of P, Au, Mn and O elements verified the successful construction of Au/BP@MnO$_2$. Meanwhile, the remarkable increases in particulate size and zeta potential determined by dynamic light scattering technique as well as the noticeable color change of the solutions further confirmed the successful functionalization of BP nanosheets. Meanwhile, the remarkable increases in particulate size (from 205.54 ± 5.91 nm to 275.03 ± 2.46 nm) and zeta potential (from −31.22 ± 3.43 to −16.61 ± 1.27 mV) determined by dynamic light scattering technique as well as the noticeable color change of the solutions further confirmed the successful functionalization of BP nanosheets (Fig. 2F and G, S2A and B, and Table S1). Moreover, Au/BP@MS kept good stability no matter in DMEM medium with 10% FBS or PBS over a period of 7 d (Fig. S2C). In addition, X-ray photoelectron spectroscopy (XPS) of Au/BP@MS confirmed the existence of Mn, O, N, C, Au, and P elements in Au/BP@MS (Fig. 2H and S3). Moreover, as shown in Fig. 2I, the peaks at 653.8 and 642.2 eV in the high-resolution Mn 2p XPS spectrum of Au/BP@MS were assigned to Mn 2p$_{1/2}$ and Mn 2p$_{3/2}$, revealing that the element Mn existed in the form of tetravalent state in Au/BP@MS [35,36]. In the Fourier transform infrared (FTIR) spectra, compared with Au/BP, the appearance of absorption bands of Mn–O, C=O, and –CH$_2$- located at 500–700, 1726, and 2923 cm^{-1} respectively also verified the successful MnO$_2$ coating and SP modification (Fig. 2J) [37,38].

The hypoxic TME would severely weaken the therapeutic efficacy of O$_2$-dependent SDT. Numerous strategies have been developed to solve this problem, such as directly transporting O$_2$ or introducing catalase-like nanoenzyme (eg, Pt NPs) [39,40]. However, the uncontrollable leakage of O$_2$ and the potentially toxic effect of metal nanoenzyme are not conducive to further clinical translation of the sonosensitizers. MnO$_2$ not only could be biodegraded in the acidic tumor microenvironment, but also has the activity similar to catalase and catalyzes the

decomposition of hydrogen peroxide (H$_2$O$_2$) to produce O$_2$, thus overcoming this dilemma and strengthening SDT efficacy [39,41]. As shown in Fig. 3A, the O$_2$ generation capability of Au/BP and Au/BP@MS in the H$_2$O$_2$ aqueous solutions was monitored by the portable dissolved oxygen meter. The dissolved O$_2$ concentration exhibited a remarkable increase in Au/BP@MS solutions with different pH but little change in pure water and Au/BP solution. Moreover, the O$_2$ generation amount of Au/BP@MS under weakly acidic solution was higher than that under neutral solution, which was due to the higher enzymatic activity of MnO$_2$ under acidic conditions.

To evaluate the capacity of sonoactivated catalytic performance of Au/BP@MS, Single Oxygen Sensor Green (SOSG), a fluorescent probe commonly used for detecting singlet oxygen (^{1}O$_2$) was employed to monitor ROS generating efficacy. As revealed in Fig. 3B and C and S4A, the characteristic absorbance of SOSG at 525 nm displayed no change in the control group while a slight increase in BP + H$_2$O$_2$ with US irradiation, but significant enhancement in Au/BP + H$_2$O$_2$ under US exposure over time, suggesting the more efficient ROS generation and the huge feasibility of Au/BP as sonosensitizers for SDT. More impressively, US-triggered ^{1}O$_2$ generating ability of Au/BP@MS was stronger than that of Au/BP at the same concentration, which would be ascribed to MnO$_2$-catalyzed H$_2$O$_2$ decomposition to supply sufficient O$_2$ as oxygen source for enhanced SDT (Fig. 3D). In addition, Au/BP@MS also showed better performance than PpIx in US-triggered ^{1}O$_2$ generation under the same concentration and US irradiation (Fig. S4B). To prove this hypothesis, the solid ultraviolet spectra of BP and Au/BP were conducted. The band gaps of BP and Au/BP were calculated to be 1.57 and 1.30 eV respectively according to the Kubelka-Munk (KM) function (Fig. 3E and F). The declined band gap of Au/BP contributed to the easier excitation by US, and the excited electrons would be effectively trapped and transferred by the anchored Au NPs, resulting in efficient separation of electron-hole pairs and enhanced generation of ROS during SDT (Fig. 3G).

As an important antioxidant, GSH is capable of scavenging excessive ROS to maintain the cellular redox homeostasis, which would also strengthen the resistance of cancer cells against oxidative stress [42,43]. Here we investigated the GSH depletion of Au/BP and Au/BP@MS using 5,5-dithiobis-(2-nitrobenzoic acid) (DTNB) as the specific probe (Fig. 3H and I, and S5). The absorbance of DTNB at 412 nm showed almost unchanged with the extension of time in control, BP and Au/BP group, while obviously decreased in Au/BP@MS, which was intuitively observed by the attenuated yellow in the photographs, illustrating that the coating of MnO$_2$ endowed Au/BP@MS with robust GSH deprivation ability. In addition to evaluating the performance and mechanism of US-triggered sonodynamic effect of Au/BP@MS nanosheets, their biodegradable behaviors in simulated TME were also studied. As shown in Fig. 3J, the structure and morphology of Au/BP@MS kept relatively intact in neutral condition for 12 h incubation while presented slight rupture after incubating in acidic buffer solution (pH = 5.5) for 3 h. However, further damage occurred in the structure of Au/BP@MS when the time extended to 6 h in the acidic buffer solution (pH = 5.5). Notably, the most serious structural collapse and dissolution of Au/BP@MS were observed after 3 h incubation in acidic reductive solution (pH = 5.5, 1 mM GSH) and almost all of the nanosheets were disintegrated at 6 h. The addition of GSH could speed up the biodegradation of the nanosheets compared to the single acidic buffer solution (pH = 5.5), indicating the excellent biodegradability of Au/BP@MS in simulated TME.

3.2. In vitro cellular uptake, cytotoxicity and SDT efficacy

Effective cellular internalization is crucial for nanomedicine to exert an anti-tumor effect, thus Au/BP@MS nanosheets were initially fluorescently labeled with near-infrared dye Cy5 and incubated with MCF-7 cancer cells for varied time points to analyze their cellular uptake using confocal scanning microscopy (CLSM) (Fig. S6A). It was found that the red fluorescence signals were mainly located around the nuclei and the
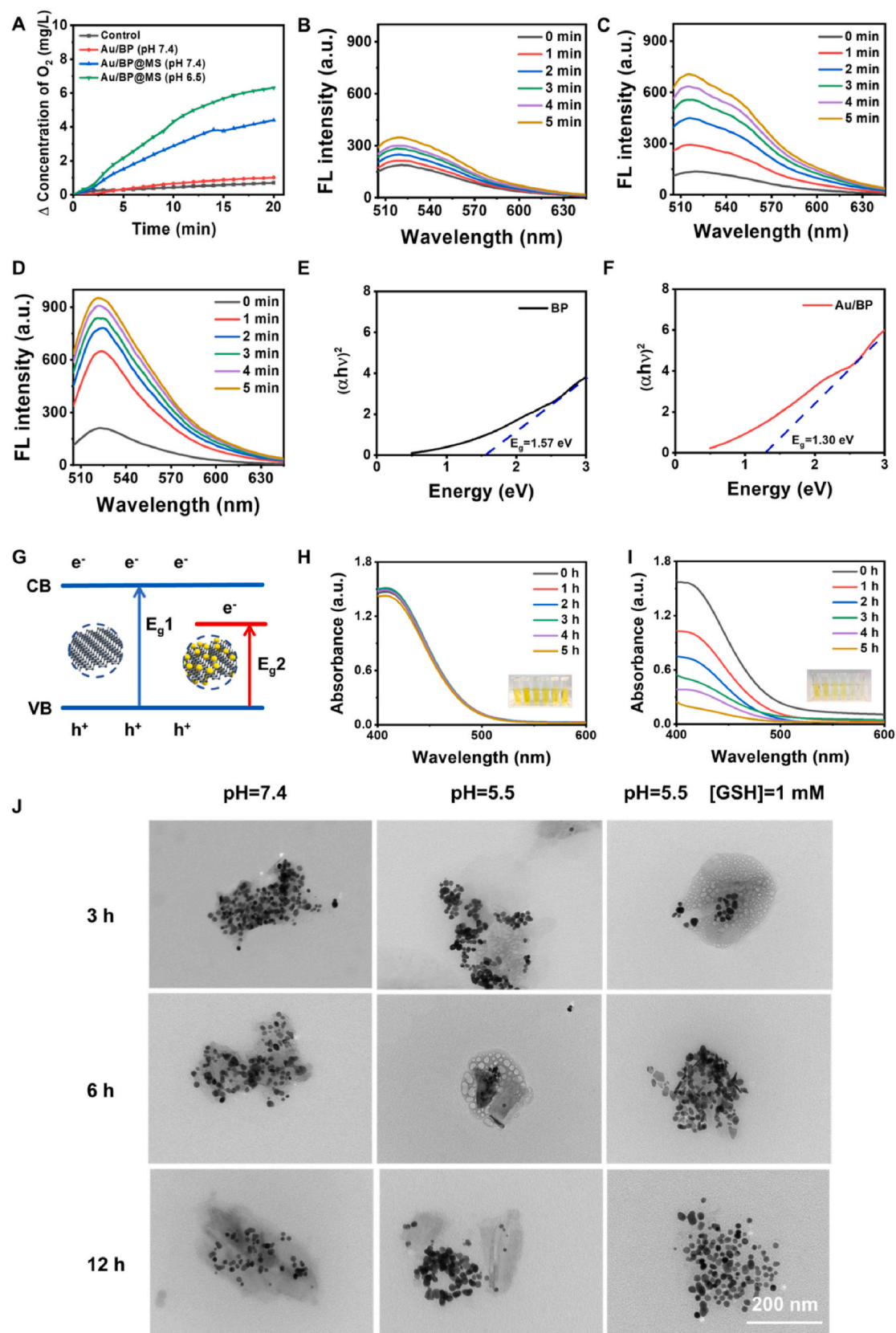
Fig. 3. *In vitro* ROS generation and GSH depletion. (A) O_2 generation in H_2O_2 solutions under different conditions. Time-dependent $^1O_2$ generation of (B) BP + H_2O_2, (C) Au/BP + H_2O_2, and (D) Au/BP@MS + H_2O_2 under US exposure using SOSG probe. Band gaps of (E) BP nanosheets and (F) Au/BP nanosheets. (G) The proposed mechanism of Au/BP@MS for enhanced SDT. (H) Au/BP and (I) Au/BP@MS-induced GSH depletion over time. Inset: the photographs of the solutions at different time points. (J) TEM images of Au/BP@MS nanosheets after incubation in pure PBS (pH = 7.4), acidic buffer solution (pH = 5.5), and acidic reductive solution (pH = 5.5, 1 mM GSH). The concentration of H_2O_2 and GSH above were 100 μM and 1.0 mM, respectively.

fluorescence intensity became stronger with the prolonged incubation time, which was also verified by the quantitative flow cytometric analysis (Fig. S6B). Next, we investigated the cytotoxicity of Au/BP and Au/BP@MS after incubation with MCF-7 cells in 24 h with or without US irradiation (Fig. 4A). The results showed that Au/BP and Au/BP@MS revealed negligible cytotoxicity to MCF-7 cells even at the concentration of 75 μg/mL, suggesting the high biocompatibility of Au/BP and Au/BP@MS nanosheets. However, the MCF-7 cell viabilities remarkably declined with the increased Au/BP concentration under US exposure, confirming the superior sonodynamic effect of Au/BP sonosensitizer. In addition, the higher cytotoxicity of Au/BP@MS + US than Au/BP + US towards MCF-7 cells further confirmed that the effective decomposition of endogenous H_2O_2 in cancer cells was beneficial to the improvement of SDT efficacy. Furthermore, the live/dead dual staining using calcein-AM and propidium iodide (PI) was also conducted to evaluate the killing effect of Au/BP@MS under US irradiation. As shown in Fig. S7, Au/BP + US would induce mild damage to MCF-7 cells due to the potent sono-sensitizing effect of Au/BP. Importantly, the sonotriggered cell-damaging effect would significantly strengthen due to the adequate supply of $^1O_2$ from Au/BP@MS + US.

To disclose the therapeutic mechanism of Au/BP@MS for enhanced SDT *in vitro*, the intracellular GSH level was assessed by incubating MCF-7 cells with BP, Au/BP, Au/BP@MS, and staining with ThiolTracker™ Violet. Compared to the control group, the green fluorescence in MCF-7 cells treated with BP and Au/BP scarcely changed while significantly declined in Au/BP@MS-treated cells, demonstrating the superior intracellular GSH depletion ability of Au/BP@MS (Fig. 4B and C). In the meantime, the O_2 generation capacity in cells was evaluated by incubating MCF-7 cells with pure DMEM, Au/BP, or Au/BP@MS for 12 h under hypoxic condition. The strong green fluorescence signal could be observed in both pure DMEM and Au/BP groups, indicating the serious hypoxic microenvironment (Fig. S8). In contrast, the green fluorescence signal was drastically decreased in Au/BP@MS group, which was similar to that of MCF-7 cells incubated with pure DMEM under normoxic condition, suggesting that the presence of MnO_2 layer in Au/BP@MS was able to produce sufficient O_2 for alleviating hypoxia due to the redox reaction between MnO_2 and endogenous H_2O_2. Inspiringly, the intracellular ROS level was subsequently determined by the 2′,7′-dichlorofluorescein diacetate (DCFH-DA) staining assay, wherein DCFH-DA has no fluorescence but could be converted into green fluorescence 2′,7′-dichloro-fluorescein (DCF) in the presence of ROS (Fig. 4D). There was almost no fluorescence in the Au/BP group, while the green fluorescence was enhanced in the Au/BP + US group due to the sonosensitizing effect of Au/BP. The weak green fluorescence in the Au/BP@MS group was because the small amount of endogenous H_2O_2 would be catalyzed to produce ROS by Au/BP@MS-mediated Fenton-like reaction. Notably, Au/BP@MS together with US irradiation exhibited the strongest green fluorescence owing to Au/BP nanosonosensitizer-involved and MnO_2-accelerated ROS generation. Subsequently, we evaluated the mitochondrial function using JC-1 dye which shows potential-dependent accumulation in mitochondria, indicated by red fluorescent J-aggregates in the normal mitochondrial membrane but green fluorescent monomers in the damaged mitochondrial membrane (Fig. 4E). It was found that in contrast to the MCF-7 cells treated with Au/BP, Au/BP@MS, or US alone, the cells treated with Au/BP + US exhibited slightly enhanced green fluorescence, suggesting that sono-triggered production of ROS could induce the decreased mitochondrial membrane potential. The strongest green fluorescence in MCF-7 cells after treatment with Au/BP@MS + US indicated the serious mitochondrial dysfunction, attributed to the most excessive elevation of intracellular oxidative stress by MnO_2-induced GSH consumption and Au/BP@MS + US-mediated ROS generation.

3.3. MR imaging and in vivo biodistribution

TME-specific biodegradation behavior of Au/BP@MS not only contributed to the excellent biocompatibility for potential clinical application, but also facilitated the abundant release of Mn^{2+} for T_1-weighted MR imaging. The longitudinal relaxivity (r_1) of Au/BP@MS in neutral condition (pH = 7.4) was 1.62 $mM^{-1}s^{-1}$ but notably increased to 7.01 $mM^{-1}s^{-1}$ in mildly acidic condition (pH = 5.5) containing 100 μM H_2O_2, suggesting that large amounts of paramagnetic Mn^{2+} could be obtained due to the decomposition of MnO_2 coating. Moreover, the r_1 value would further rise to 9.43 $mM^{-1}s^{-1}$ after the addition of 10 mM GSH, illustrating that GSH was conducive to the production of Mn^{2+} (Fig. 5A and B). *In vivo* MR imaging of the mice bearing MCF-7 tumor was then assessed by intravenous (i.v.) administration of Au/BP@MS. It was found that the tumor site became illuminated at 24 h post-injection, indicating that Au/BP@MS could be effectively accumulated in the tumor area and reduced to Mn^{2+} by tumor-specific microenvironment for enhanced T_1-weighted MR imaging. The MR signal intensity at the tumor site after 24 h injection was approximately 1.41-fold higher than that before injection, while the MR signal intensity of the surrounding muscles revealed no obvious changes before and after injection (Fig. 5C and D). Subsequently, the *in vivo* biodistribution of Au/BP@MS was evaluated by i.v. injection of Au/BP@MS-Cy5 in MCF-7 tumor-bearing mice and tracking the fluorescence signals at different time points (Fig. 5E). In comparison with free Cy5 group, the stronger fluorescence signals could be observed in the tumor site in Au/BP@MS-Cy5 group. Moreover, the fluorescence intensity intensified over time and reached its maximum at 12 h post-injection (Fig. S9). The *ex vivo* fluorescence images further verified that Au/BP@MS were mainly accumulated in the tumor tissue other than other major organs, including heart, liver, spleen, lung, and kidney (Fig. 5F and G).

3.4. In vivo antitumor efficacy

Encouraged by the excellent sonocatalytic tumor treatment of Au/BP@MS *in vitro*, we further evaluated their efficacy *in vivo* against mice bearing MCF-7 tumor. As can be seen from Fig. 6A–C, the mice bearing tumor were randomly separated into six groups and intravenously injected with PBS, PBS + US, Au/BP, Au/BP + US, Au/BP@MS, and Au/BP@MS + US. In the groups with US irradiation, the tumor areas of mice were irradiated with US (1 MHz, 1.0 W/cm², 50% duty cycle, 5 min) at 12 h post-injection and repeated for three treatments. During the period of treatment, the tumor volume and body weight were monitored every two days. It was notable that the tumor growth was slightly suppressed in Au/BP + US group while significantly inhibited in Au/BP@MS + US group, suggesting that Au/BP@MS could induce potent sonotoxicity via the amplification of intratumoral oxidative stress under US exposure. The hematoxylin and eosin (H&E) and terminal deoxynucleotidyl transferase-mediated dUTP nick end labeling (TUNEL) immunofluorescence staining of tumor slices further verified the most notable cellular damage and apoptosis in Au/BP@MS + US group (Fig. 6D). Moreover, the tumor hypoxic status in each group was further evaluated by immunofluorescence staining to determine the expressions of hypoxia-inducible factor 1α/vascular endothelial growth factor (HIF-1α/VEGF) (Fig. 6E). The strong fluorescence signals of HIF-1α (red) and VEGF (green) in control, US alone, Au/BP, and Au/BP + US groups revealed the severe hypoxia levels in tumor tissues. Comparatively, the attenuated fluorescence signals of HIF-1α and VEGF could be distinctly observed in Au/BP@MS and Au/BP@MS + US groups, attributed to the sufficient O_2 generation from endogenous H_2O_2 catalyzed by MnO_2 layer in Au/BP@MS. The alleviated hypoxic level in Au/BP@MS + US was beneficial for promoting *in vivo* SDT therapeutic performance and reducing hypoxia-associated resistance in oncology therapy. In addition, no obvious difference in body weight and histopathological change in major organs (heart, liver, kidney, lung, and spleen) were observed in all treatment groups compared to the control group, showing the high biosafety of these treatment modalities (Figs. S10 and S11).
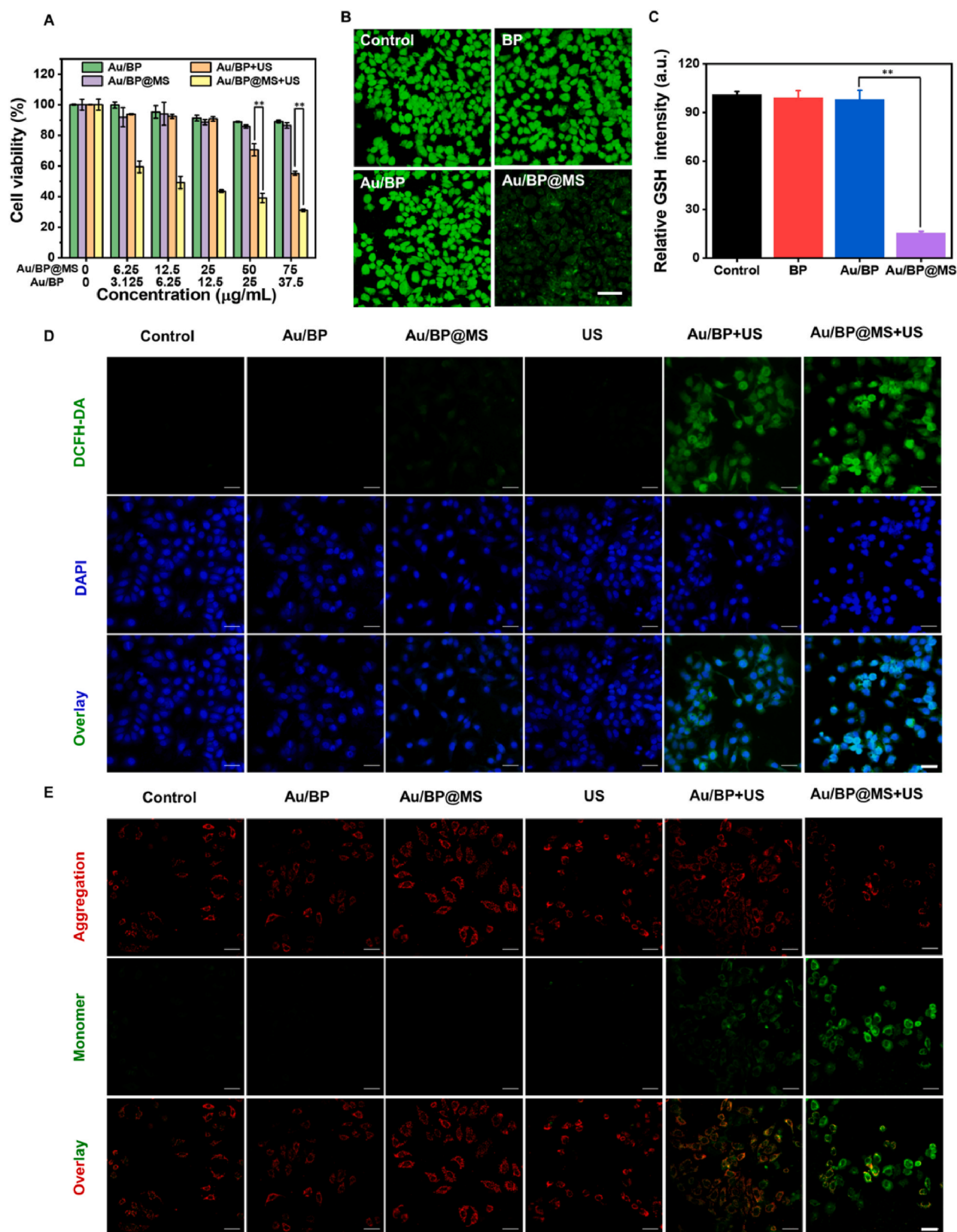
Fig. 4. *In vitro* cytotoxicity and SDT efficacy. (A) Relative cell viabilities of MCF-7 cells after treatment with Au/BP and Au/BP@MS at varied concentrations with or without US irradiation in 24 h incubation. (B) CLSM images and (C) quantification of intracellular GSH depletion in MCF-7 cells stained with ThiolTracker™ Violet (green) after incubation with BP, Au/BP, and Au/BP@MS nanosheets. Scale bar = 50 μm. (D) CLSM images of intracellular ROS level in MCF-7 cells after receiving different treatments. Scale bar = 50 μm. (E) CLSM images of the mitochondrial membrane potential in MCF-7 cells after varied treatments indicated by JC-1 monomer (green channel) and aggregate (red channel). Scale bar = 50 μm. *p* values in (A) and (C) were calculated by Tukey's post-test (***$p < 0.001$, **$p < 0.01$, or *$p < 0.05$).
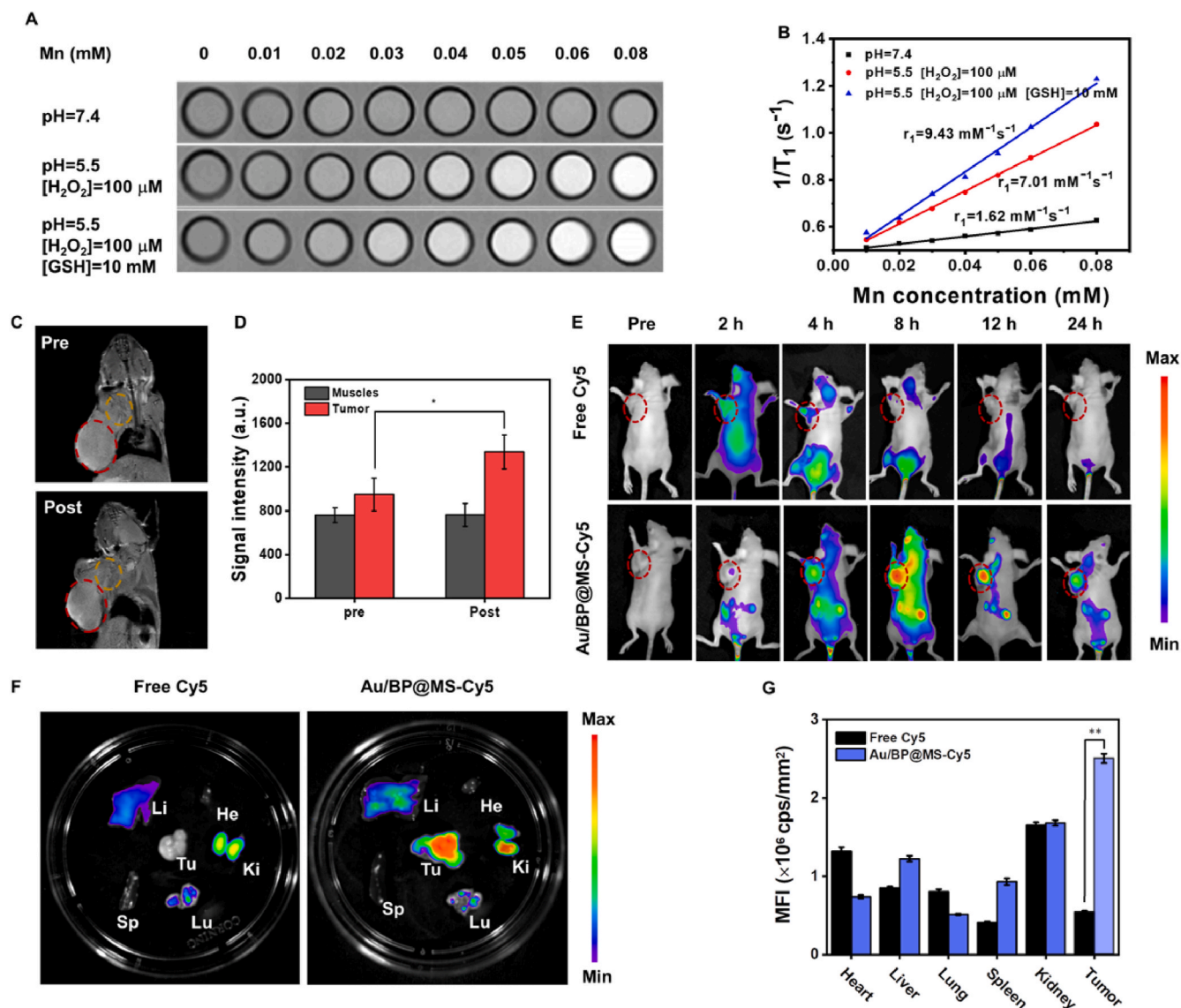
Fig. 5. MR imaging and *in vivo* biodistribution. (A) T_1-weighted MR imaging and (B) corresponding T_1^{-1} versus Mn concentration for different concentrations of Au/BP@MS under varied conditions. (C) *In vivo* MR imaging and (D) quantification and of MCF-7 tumor-bearing mice before and after i.v. injection of Au/BP@MS at 24 h. The red circles indicate the tumor region. The yellow circles indicate the surrounding muscle region. (E) Time-dependent *in vivo* fluorescence imaging of MCF-7 tumor-bearing mice post i.v. injection of free Cy5 and Cy5-labeled Au/BP@MS. The red circles indicate the tumor region. (F) *Ex vivo* fluorescence image of the tumor and major organs from the free Cy5-treated and Cy5-labeled Au/BP@MS-treated mice at 24 h post-injection. (G) Quantitative biodistribution analysis of the tumor and major organs from the free Cy5-treated and Cy5-labeled Au/BP@MS-treated mice at 24 h post-injection. *p* values in (D) and (G) were calculated by Tukey's post-test (***$p < 0.001$, **$p < 0.01$, or *$p < 0.05$).

4. Conclusions

In summary, we fabricated a novel kind of US-triggered tumor theranostic nanoplatforms by integrating Au NPs and MnO_2 with biocompatible/biodegradable ultrathin 2D BP nanosheets. The anchored Au NPs on BP nanosheets could decrease the band gap of BP and trap the excited electrons, thus improving the separation of electron-hole pairs for enhanced sonodynamic effect. Moreover, the introduced MnO_2 could decompose endogenous H_2O_2 to provide adequate O_2 and consume GSH in TME, amplifying the intratumoral oxidative stress. Notably, the tumor growth would be efficiently suppressed in Au/BP@MS together with US irradiation. The high biodegradability of Au/BP@MS not only guaranteed their possible clinical translation but also supplied abundant Mn^{2+} for tumor-specific MR imaging. This work has exploited the enormous potential of Au/BP as promising sonosensitizers, which also provides a new perspective for the evolution of BP-based tumor theranostic nanoplatforms.

CRediT authorship contribution statement

Ting Chen: Conceptualization, Data curation, Investigation, Methodology, Writing – original draft. **Weiwei Zeng:** Investigation, Methodology, Writing – original draft. **Changjun Tie:** Data curation, Formal analysis. **Mian Yu:** Investigation, Data curation. **Huisong Hao:** Investigation, Data curation. **Yang Deng:** Validation, Data curation. **Qianqian Li:** Validation, Data curation. **Hairong Zheng:** Resources, Supervision. **Meiying Wu:** Supervision, Funding acquisition, Project administration, Writing – review & editing. **Lin Mei:** Supervision, Funding acquisition, Project administration, Writing – review & editing.
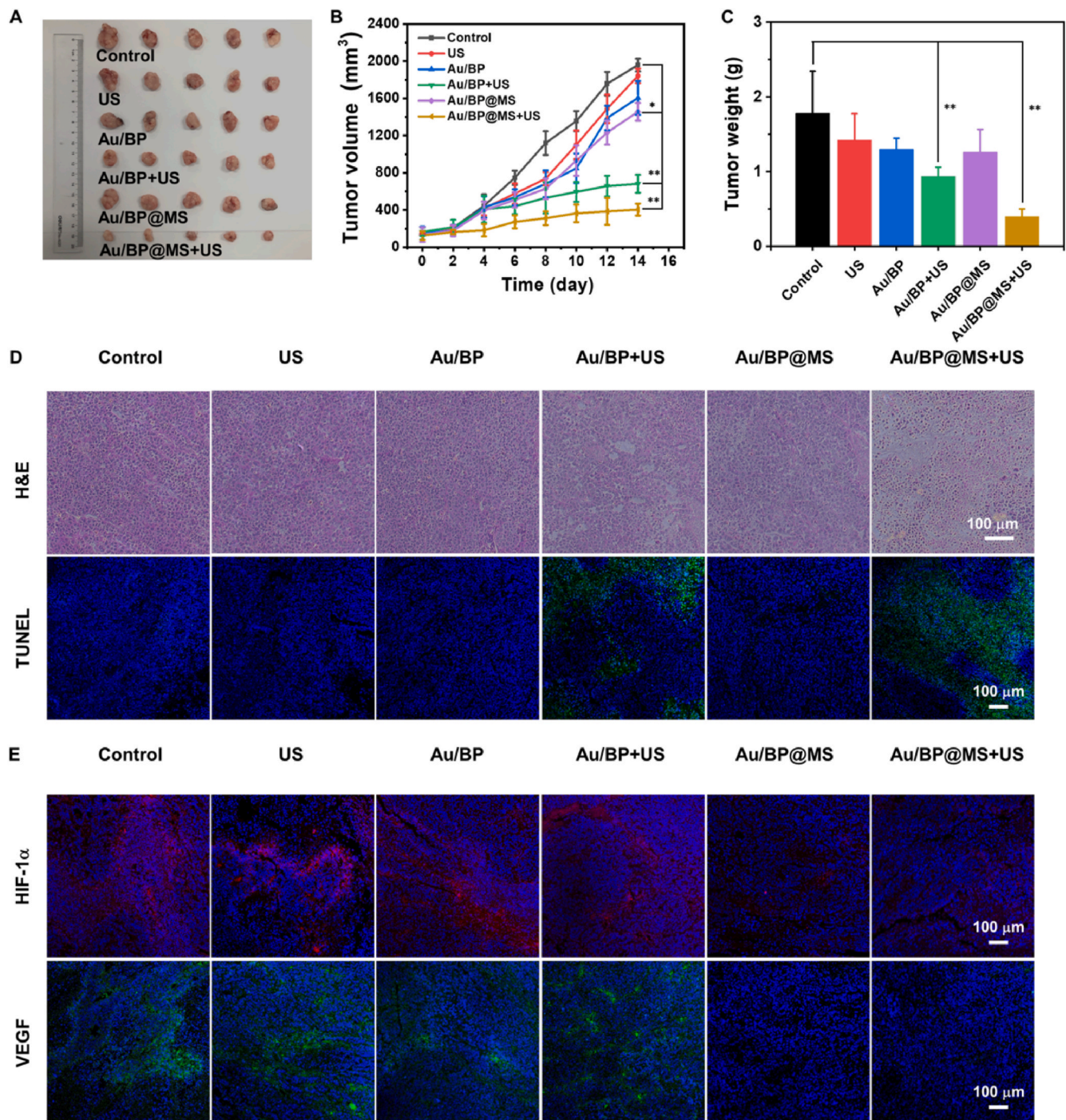
Fig. 6. *In vivo* therapeutic efficacy. (A) Representative image of tumors collected from mice received PBS, PBS + US, Au/BP, Au/BP + US, Au/BP@MS, and Au/BP@MS + US on day 14. (B) Relative tumor volume curves of the mice in each experimental group during treatment. (C) Tumor weights of mice bearing MCF-7 tumor after various treatments (n = 5). (D) H&E staining and TUNEL immunofluorescence staining of tumor slices in each group after different therapies. (E) Immunofluorescence images of hypoxia areas stained with HIF-1α (red) and VEGF (green). *p* values in (B) and (C) were calculated by Tukey's post-test (***$p < 0.001$, **$p < 0.01$, or *$p < 0.05$).

Declaration of competing interest

The authors declare that they have no known competing financial interests or personal relationships that could have appeared to influence the work reported in this paper.

Acknowledgments

Appendix A. Supplementary data

Supplementary data to this article can be found online at https://doi.org/10.1016/j.bioactmat.2021.09.016.

References

[1] D. Trachootham, J. Alexandre, P. Huang, Targeting cancer cells by ROS-mediated mechanisms: a radical therapeutic approach? Nat. Rev. Drug Discov. 8 (2009) 579–591.

[2] C. Gorrini, I.S. Harris, T.W. Mak, Modulation of oxidative stress as an anticancer strategy, Nat. Rev. Drug Discov. 12 (2013) 931–947.

[3] W. Zeng, X. Wu, T. Chen, S. Sun, Z. Shi, J. Liu, X. Ji, X. Zeng, J. Guan, L. Mei, M. Wu, Renal-clearable ultrasmall polypyrrole nanoparticles with size-regulated property for second near-infrared light-mediated photothermal therapy, Adv. Funct. Mater. 31 (2021) 2008362.

[4] Y. Yang, W. Zeng, P. Huang, X. Zeng, L. Mei, Smart materials for drug delivery and cancer therapy, View 2 (2020).

[5] J. Noh, B. Kwon, E. Han, M. Park, W. Yang, W. Cho, W. Yoo, G. Khang, D. Lee, Amplification of oxidative stress by a dual stimuli-responsive hybrid drug enhances cancer cell death, Nat. Commun. 6 (2015) 6907.

[6] I. Rosenthal, J.Z. Sostaric, P. Riesz, Sonodynamic therapy–a review of the synergistic effects of drugs and ultrasound, Ultrason. Sonochem. 11 (2004) 349–363.

[7] P. Zhu, Y. Chen, J. Shi, Nanoenzyme-augmented cancer sonodynamic therapy by catalytic tumor oxygenation, ACS Nano 12 (2018) 3780–3795.

[8] S. Sun, M. Wu, Sonodynamic Therapy: another "light" in tumor treatment by exogenous stimulus, Smart Mater. Med. 2 (2021) 142–149.

[9] X. Qian, Y. Zheng, Y. Chen, Micro/Nanoparticle-augmented sonodynamic therapy (SDT): breaking the depth shallow of photoactivation, Adv. Mater. 28 (2016) 8097–8129.

[10] X. Pan, L. Bai, H. Wang, Q. Wu, H. Wang, S. Liu, B. Xu, X. Shi, H. Liu, Metal–organic-framework-derived carbon nanostructure augmented sonodynamic cancer therapy, Adv. Mater. 30 (2018) 1800180.

[11] P. Huang, X. Qian, Y. Chen, L. Yu, H. Lin, L. Wang, Y. Zhu, J. Shi, Metalloporphyrin-encapsulated biodegradable nanosystems for highly efficient magnetic resonance imaging-guided sonodynamic cancer therapy, J. Am. Chem. Soc. 139 (2017) 1275–1284.

[12] A. Ma, H. Chen, Y. Cui, Z. Luo, R. Liang, Z. Wu, Z. Chen, T. Yin, J. Ni, M. Zheng, L. Cai, Metalloporphyrin complex-based nanosonosensitizers for deep-tissue tumor theranostics by noninvasive sonodynamic therapy, Small 15 (2018) e1804028.

[13] A. Takai, M. Chkounda, A. Eggenspiller, C.P. Gros, M. Lachkar, J.M. Barbe, S. Fukuzumi, Efficient photoinduced electron transfer in a porphyrin tripod-fullerene supramolecular complex via pi-pi interactions in nonpolar media, J. Am. Chem. Soc. 132 (2010) 4477–4489.

[14] K. Liang, Z. Li, Y. Luo, Q. Zhang, F. Yin, L. Xu, H. Chen, H. Wang, Intelligent nanocomposites with intrinsic blood–brain-barrier crossing ability designed for highly specific MR imaging and sonodynamic therapy of glioblastoma, Small 16 (2020) 1906985.

[15] D.G. You, V.G. Deepagan, W. Um, S. Jeon, S. Son, H. Chang, H.I. Yoon, Y.W. Cho, M. Swierczewska, S. Lee, M.G. Pomper, I.C. Kwon, K. Kim, J.H. Park, ROS-generating TiO₂ nanoparticles for non-invasive sonodynamic therapy of cancer, Sci. Rep. 6 (2016) 23200.

[16] C. Dai, S. Zhang, Z. Liu, R. Wu, Y. Chen, Two-dimensional graphene augments nanosonosensitized sonocatalytic tumor eradication, ACS Nano 11 (2017) 9467–9480.

[17] Z. Sun, H. Xie, S. Tang, X.F. Yu, Z. Guo, J. Shao, H. Zhang, H. Huang, H. Wang, P. K. Chu, Ultrasmall black phosphorus quantum dots: synthesis and use as photothermal agents, Angew. Chem. Int. Ed. 54 (2015) 11526–11530.

[18] J. Shao, H. Xie, H. Huang, Z. Li, Z. Sun, Y. Xu, Q. Xiao, X.F. Yu, Y. Zhao, H. Zhang, H. Wang, P.K. Chu, Biodegradable black phosphorus-based nanospheres for in vivo photothermal cancer therapy, Nat. Commun. 7 (2016) 12967.

[19] M. Luo, T. Fan, Y. Zhou, H. Zhang, L. Mei, 2D black phosphorus–based biomedical applications, Adv. Funct. Mater. 29 (2019).

[20] C. Lin, H. Hao, L. Mei, M. Wu, Metal-free two-dimensional nanomaterial-mediated photothermal tumor therapy, Smart Mater. Med. 1 (2020) 150–167.

[21] W. Chen, J. Ouyang, H. Liu, M. Chen, K. Zeng, J. Sheng, Z. Liu, Y. Han, L. Wang, J. Li, L. Deng, Y.N. Liu, S. Guo, Black phosphorus nanosheet-based drug delivery system for synergistic photodynamic/photothermal/chemotherapy of cancer, Adv. Mater. 29 (2017).

[22] W. Tao, X. Zhu, X. Yu, X. Zeng, Q. Xiao, X. Zhang, X. Ji, X. Wang, J. Shi, H. Zhang, L. Mei, Black phosphorus nanosheets as a robust delivery platform for cancer theranostics, Adv. Mater. 29 (2017).

[23] X. Zeng, M. Luo, G. Liu, X. Wang, W. Tao, Y. Lin, X. Ji, L. Nie, L. Mei, Polydopamine-modified black phosphorous nanocapsule with enhanced stability and photothermal performance for tumor multimodal treatments, Adv. Sci. 5 (2018) 1800510.

[24] Z. Li, T. Zhang, F. Fan, F. Gao, H. Ji, L. Yang, Piezoelectric materials as sonodynamic sensitizers to safely ablate tumors: a case study using black phosphorus, J. Phys. Chem. Lett. 11 (2020) 1228–1238.

[25] X. Guan, H.-H. Yin, X.-H. Xu, G. Xu, Y. Zhang, B.-G. Zhou, W.-W. Yue, C. Liu, L.-P. Sun, H.-X. Xu, K. Zhang, Tumor metabolism-engineered composite nanoplatforms potentiate sonodynamic therapy via reshaping tumor microenvironment and facilitating electron–hole pairs' separation, Adv. Funct. Mater. 30 (2020) 2000326.

[26] G. Yang, L. Xu, Y. Chao, J. Xu, X. Sun, Y. Wu, R. Peng, Z. Liu, Hollow MnO₂ as a tumor-microenvironment-responsive biodegradable nano-platform for combination therapy favoring antitumor immune responses, Nat. Commun. 8 (2017) 902.

[27] H. Zhang, W. Zeng, C. Pan, L. Feng, M. Ou, X. Zeng, X. Liang, M. Wu, X. Ji, L. Mei, SnTe@MnO₂-SP nanosheet–based intelligent nanoplatform for second near-infrared light–mediated cancer theranostics, Adv. Funct. Mater. 29 (2019).

[28] W. Zeng, H. Zhang, Y. Deng, A. Jiang, X. Bao, M. Guo, Z. Li, M. Wu, X. Ji, X. Zeng, L. Mei, Dual-response oxygen-generating MnO₂ nanoparticles with polydopamine modification for combined photothermal-photodynamic therapy, Chem. Eng. J. 389 (2020).

[29] M. Zhu, S. Kim, L. Mao, M. Fujitsuka, J. Zhang, X. Wang, T. Majima, Metal-free photocatalyst for H₂ evolution in visible to near-infrared region: black phosphorus/graphitic carbon nitride, J. Am. Chem. Soc. 139 (2017) 13234–13242.

[30] V.G. Deepagan, D.G. You, W. Um, H. Ko, S. Kwon, K.Y. Choi, G.R. Yi, J.Y. Lee, D. S. Lee, K. Kim, I.C. Kwon, J.H. Park, Long-circulating Au-TiO₂ nanocomposite as a sonosensitizer for ROS-mediated eradication of cancer, Nano Lett. 16 (2016) 6257–6264.

[31] J. Ouyang, L. Deng, W. Chen, J. Sheng, Z. Liu, L. Wang, Y.N. Liu, Two dimensional semiconductors for ultrasound-mediated cancer therapy: the case of black phosphorus nanosheets, Chem. Commun. 54 (2018) 2874–2877.

[32] L.S. Lin, J. Song, L. Song, K. Ke, Y. Liu, Z. Zhou, Z. Shen, J. Li, Z. Yang, W. Tang, G. Niu, H.H. Yang, X. Chen, Simultaneous fenton-like ion delivery and glutathione depletion by MnO₂ -based nanoagent to enhance chemodynamic therapy, Angew. Chem. Int. Ed. Engl. 57 (2018) 4902–4906.

[33] F. Gao, X. Yang, X. Luo, X. Xue, C. Qian, M. Sun, Photoactivated nanosheets accelerate nucleus access of cisplatin for drug-resistant cancer therapy, Adv. Funct. Mater. 30 (2020).

[34] T. He, C. Jiang, J. He, Y. Zhang, G. He, J. Wu, J. Lin, X. Zhou, P. Huang, Manganese-dioxide-coating-instructed plasmonic modulation of gold nanorods for activatable duplex-imaging-guided NIR-II photothermal-chemodynamic therapy, Adv. Mater. 33 (2021), e2008540.

[35] W. Zhu, Z. Dong, T. Fu, J. Liu, Q. Chen, Y. Li, R. Zhu, L. Xu, Z. Liu, Modulation of hypoxia in solid tumor microenvironment with MnO₂ nanoparticles to enhance photodynamic therapy, Adv. Funct. Mater. 26 (2016) 5490–5498.

[36] Q. Wu, G. Chen, K. Gong, J. Wang, X. Ge, X. Liu, S. Guo, F. Wang, MnO₂-laden black phosphorus for MRI-guided synergistic PDT, PTT, and chemotherapy, Matter 1 (2019) 496–512.

[37] W. Fan, W. Bu, B. Shen, Q. He, Z. Cui, Y. Liu, X. Zheng, K. Zhao, J. Shi, Intelligent MnO₂ nanosheets anchored with upconversion nanoprobes for concurrent pH-/H₂O₂-responsive UCL imaging and oxygen-elevated synergetic therapy, Adv. Mater. 27 (2015) 4155–4161.

[38] A.E. Elshafie, S.J. Joshi, Y.M. Al-Wahaibi, A.S. Al-Bemani, S.N. Al-Bahry, D.a. Al-Maqbali, I.M. Banat, Sophorolipids production by candida bombicola ATCC 22214 and its potential application in microbial enhanced oil recovery, Front. Microbiol. 6 (2015).

[39] J. Chen, H. Luo, Y. Liu, W. Zhang, H. Li, T. Luo, K. Zhang, Y. Zhao, J. Liu, Oxygen-self-produced nanoplatform for relieving hypoxia and breaking resistance to sonodynamic treatment of pancreatic cancer, ACS Nano 11 (2017) 12849–12862.

[40] S. Liang, X. Deng, Y. Chang, C. Sun, S. Shao, Z. Xie, X. Xiao, P. Ma, H. Zhang, Z. Cheng, J. Lin, Intelligent hollow Pt-CuS janus architecture for synergistic catalysis-enhanced sonodynamic and photothermal cancer therapy, Nano Lett. 19 (2019) 4134–4145.

[41] G. Li, S. Wang, D. Deng, Z. Xiao, Z. Dong, Z. Wang, Q. Lei, S. Gao, G. Huang, E. Zhang, G. Zeng, Z. Wen, S. Wu, Z. Liu, Fluorinated chitosan to enhance transmucosal delivery of sonosensitizer-conjugated catalase for sonodynamic bladder cancer treatment post-intravesical instillation, ACS Nano 14 (2020) 1586–1599.

[42] P. Sun, Q. Deng, L. Kang, Y. Sun, J. Ren, X. Qu, A smart nanoparticle-laden and remote-controlled self-destructive macrophage for enhanced chemo/chemodynamic synergistic therapy, ACS Nano 14 (2020) 13894–13904.

[43] F. Zhang, G. Lu, X. Wen, F. Li, X. Ji, Q. Li, M. Wu, Q. Cheng, Y. Yu, J. Tang, L. Mei, Magnetic nanoparticles coated with polyphenols for spatio-temporally controlled cancer photothermal/immunotherapy, J. Contr. Release 326 (2020) 131–139.